NASA/TM–20250008678

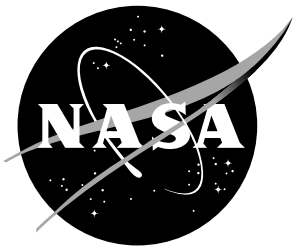

Development of a Rapid Controls Prototyping Testbed For Wing-Mounted Distributed Electric Propulsion Arrays

Vincent A. Spada, Elyse Hill, Benjamin M. Simmons, and Ryan Chan
Langley Research Center, Hampton, Virginia

December 2025

NASA STI Program Report Series

Since its founding, NASA has been dedicated to the advancement of aeronautics and space science. The NASA scientific and technical information (STI) program plays a key part in helping NASA maintain this important role.

The NASA STI program operates under the auspices of the Agency Chief Information Officer. It collects, organizes, provides for archiving, and disseminates NASA's STI. The NASA STI program provides access to the NTRS Registered and its public interface, the NASA Technical Reports Server, thus providing one of the largest collections of aeronautical and space science STI in the world. Results are published in both non-NASA channels and by NASA in the NASA STI Report Series, which includes the following report types:

- TECHNICAL PUBLICATION. Reports of completed research or a major significant phase of research that present the results of NASA Programs and include extensive data or theoretical analysis. Includes compilations of significant scientific and technical data and information deemed to be of continuing reference value. NASA counterpart of peer-reviewed formal professional papers but has less stringent limitations on manuscript length and extent of graphic presentations.
- TECHNICAL MEMORANDUM. Scientific and technical findings that are preliminary or of specialized interest, e.g., quick release reports, working papers, and bibliographies that contain minimal annotation. Does not contain extensive analysis.
- CONTRACTOR REPORT. Scientific and technical findings by NASA-sponsored contractors and grantees.
- CONFERENCE PUBLICATION. Collected papers from scientific and technical conferences, symposia, seminars, or other meetings sponsored or co-sponsored by NASA.
- SPECIAL PUBLICATION. Scientific, technical, or historical information from NASA programs, projects, and missions, often concerned with subjects having substantial public interest.
- TECHNICAL TRANSLATION. English-language translations of foreign scientific and technical material pertinent to NASA's mission.

Specialized services also include organizing and publishing research results, distributing specialized research announcements and feeds, providing information desk and personal search support, and enabling data exchange services.

For more information about the NASA STI program, see the following:

- Access the NASA STI program home page at http://www.sti.nasa.gov
- Help desk contact information:

https://www.sti.nasa.gov/sti-contact-form/ and select the "General" help request type.

NASA/TM–20250008678

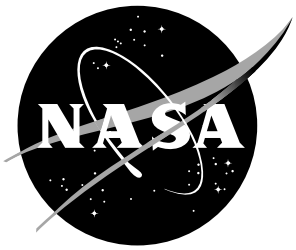

Development of a Rapid Controls Prototyping Testbed For Wing-Mounted Distributed Electric Propulsion Arrays

Vincent A. Spada, Elyse Hill, Benjamin M. Simmons, and Ryan Chan
Langley Research Center, Hampton, Virginia

National Aeronautics and
Space Administration

Langley Research Center
Hampton, Virginia 23681-2199

December 2025

Available from:

NASA STI Program / Mail Stop 148
NASA Langley Research Center
Hampton, VA 23681-2199
Fax: 757-864-6500

Abstract

The Hardware Integrated Controls and Avionics Testbed (HICAT) enables rapid prototyping and testing of avionics and control algorithms for wing-mounted distributed electric propulsion (DEP) systems. Capabilities of the rig include vehicle-like command-and-data-handling (C&DH) hardware, a high power capacity, and a flight dynamics simulation environment based on wind tunnel and flight test data to facilitate system-level testing. HICAT, modeled on a proposed DEP design for a next-generation transport aircraft, can study component layout, wiring, C&DH routines, and control strategies at motor and vehicle levels. To validate the DEP array design concept, thrust response and velocity tracking metrics were gathered using a flight dynamics simulation. The flight dynamics simulation communicates with real propulsion hardware to evaluate the propulsion system performance as if it were being used on a real aircraft. These results demonstrate the capability of HICAT to rapidly transition conceptual designs to operational hardware prototypes for high-power flight control systems.

Contents

List of Figures

Nomenclature

Symbols

b	wing span, ft
$\bar{c}$	mean aerodynamic chord, ft
C_l	aerodynamic rolling moment coefficient
C_m	aerodynamic pitching moment coefficient
C_n	aerodynamic yawing moment coefficient
C_X	aerodynamic longitudinal force coefficient
C_Y	aerodynamic lateral force coefficient
C_Z	aerodynamic vertical force coefficient
g	acceleration due to gravity, ft/s^2
I_x, I_y, I_z, I_{xz}	moments of inertia, slug·ft^2
K	gain matrix
n_{fan}	number of fans
p, q, r	body-axis angular velocity components, rad/s or deg/s
$\hat{p}, \hat{q}, \hat{r}$	nondimensional roll rate ($pb/2V$), pitch rate ($q\bar{c}/2V$), and yaw rate ($rb/2V$)
$\bar{q}$	dynamic pressure ($\rho V^2/2$), lbf/ft^2
Q, R	weighting matrices
S	wing area, ft^2
T	thrust, lbf
$\mathbf{u}$	system input
u, v, w	body-axis translational velocity components, ft/s
V_t	true airspeed, ft/s
$\mathbf{x}$	system state
x_E, y_E, z_E	Earth-fixed position, ft
α	angle of attack, deg or rad
β	sideslip angle, deg or rad
δ_a	aileron deflection angle, deg or rad
δ_e	elevator deflection angle, deg or rad
δ_f	flap deflection angle, deg or rad
δ_r	rudder deflection angle, deg or rad
ρ	air density, slug/ft^3
ϕ, θ, ψ	Euler roll, pitch, and yaw angles, rad or deg

Superscripts

$\dot{\cdot}$	time derivative

Subscripts

$\cdot_{\text{act}}$	actual variable

$_{cmd}$	commanded variable
$_{e}$	error variable
$_{lat}$	lateral-directional variable
$_{lon}$	longitudinal variable
$_{ref}$	reference variable
$_{trim}$	trim variable

Acronyms

CAN	Controller Area Network
CAN HS	High-Speed CAN
C&DH	Command and Data Handling
CRM	Common Research Model
DCU	Distributed Control Unit
DEP	Distributed Electric Propulsion
EDF	Electric Ducted Fan
EMI	Electromagnetic Interference
ESC	Electronic Speed Controller
HICAT	Hardware Integrated Controls and Avionics Testbed
IC	Integrated Circuit
ID	Identification Number
I/O	Input/Output
ISO	International Organization for Standardization
LQR	Linear Quadratic Regulator
PAI	Propulsion-Airframe Integration
PCB	Printed Circuit Board
PI	Proportional Integral
PS	Power Supply
PWM	Pulse-Width Modulation
SAE	Society of Automobile Engineers
SITL	Software-In-The-Loop
SUSAN	SUbsonic Single Aft-eNgine electrofan
T/W	Thrust to Weight Ratio
UART	Universal Asynchronous Receiver/Transmitter
VAC	Voltage Alternating Current
VDC	Voltage Direct Current
VMC	Vehicle Management Computer

1 Introduction

Aircraft flight control systems often convert pilot inputs from the inceptors into electronic command signals sent to control surfaces and propulsion units. Because aircraft subsystems are complex electromechanical devices, they exhibit physical and computational constraints. Subsystem characteristics influence flight control system performance, requiring algorithms to be tailored to specific hardware. Consequently, engineers make use of ground-based "iron-bird" rigs (i.e., aircraft system testbeds) to resolve subsystem-to-system nuances and validate control performance prior to flight.

Subsystem prototypes can be tested with partial system-level interactions in the loop before a complete iron-bird is built. This report documents the performance evaluation of a distributed electric propulsion (DEP) array with certain important system integration effects in the loop. The rig used for testing, termed the Hardware Integrated Controls and Avionics Testbed (HICAT), consists of a vehicle management computer (VMC), and four electric ducted fans (EDF) arranged in an array with preliminary components for a future thrust vectoring system on each fan. The VMC hosts a flight dynamics simulation and a control algorithm, and connects to the EDFs and thrust vectoring hardware. The EDFs and thrust vectoring hardware comprise a portion of the overall DEP system, and are used to emulate the full system in the VMC-hosted simulation. The system is designated as a "rapid" prototyping testbed to highlight the ability to iteratively develop hardware and algorithms during testing.

This work contributes to research for NASA's Subsonic Single Aft Engine (SUSAN) Electrofan project, which studied a hybrid-electric commercial transport concept aircraft with DEP arrays located under the wings near the trailing edge. Trade studies and computational fluid dynamics simulations for SUSAN suggested that wing-mounted DEP arrays are advantageous for aerodynamic performance and structural layout [1–3]. Subsequent computational refinements are described in Refs. [4, 5]. Power architecture studies in Refs. [6–8] led to the selection of a hybrid-electric system featuring an aft-mounted turbofan for thrust and power generation. The SUSAN project also began development of a subscale flight research vehicle that resembled the full-scale concept aircraft [9, 10]. The flight research vehicle is similar to a quarter-scale model of a Boeing 737 with a wingspan around 30 ft. Beyond conceptual work, Ref. [11] documents a wind tunnel test campaign conducted to characterize an EDF proposed for use on the DEP arrays on the subscale vehicle. The test measured the EDF's thrust and electrical performance independently of system integration effects. Another wind tunnel test, documented in Ref. [12], examined propulsion-airframe integration (PAI) effects and demonstrated that blowing airflow over lifting surfaces can augment lift. The work described herein extends progress made by the SUSAN project by including preliminary thrust vectoring hardware, flight-like embedded systems, a realistic component layout, a flight dynamics model, and controls for closed-loop simulation.

The remainder of this report is organized as follows: Section 2 provides an overview of the investigated hardware, and is followed by a detailed description of specifications in Section 3. Simulation setup and flight control are presented in Section 4 and Section 5, respectively. Verification results are discussed in Section 6, and conclusions are summarized in Section 7. This report is a closeout deliverable for the Agile Distributed Electric Propulsion Technologies (ADEPT) study that was prematurely ended due to the Convergent Aeronautics Solutions (CAS) project being discontinued in September 2025. Consequently, some of the material in this report is preliminary in nature and could be expanded in future work.

2 Hardware Overview

The HICAT rig consists of power distribution components, a VMC, four EDFs with motor drivers, and two control motors with drivers for each EDF intended to be used for thrust vectoring. The EDFs, thrust vectoring mechanism motors, motor drivers, and communication circuits form an EDF Control Unit (ECU) seen in Fig. 1. The SUSAN subscale vehicle is proposed to use eight ECUs in each DEP array mounted to the trailing edge, inboard section of each wing. This section covers the HICAT design rationale, including power bus specifications and thrust requirements, tied to the design of the flight research vehicle by introducing each component of the testbed. A rendering of the four ECUs used on the HICAT layout can be seen in Fig. 1.

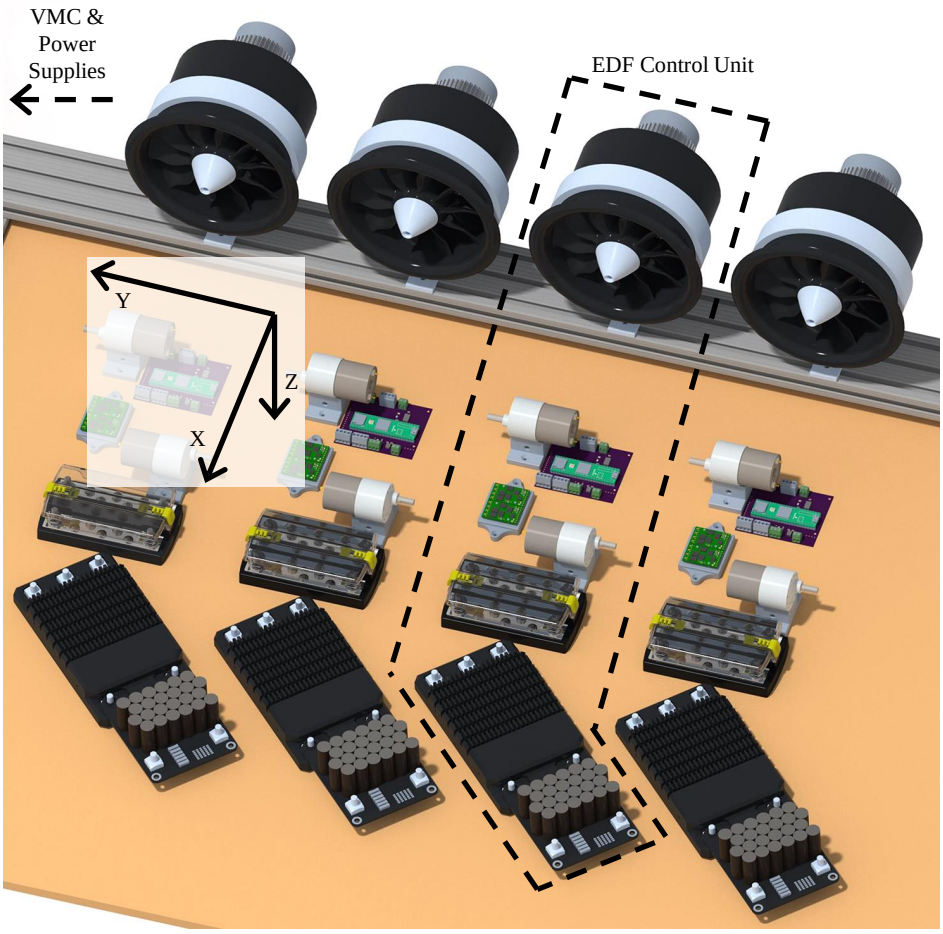

Figure 1: HICAT assembly with body coordinate system and four EDF Control Units. The power system and VMC are located to the left out of view.

A Speedgoat® real-time machine is the VMC for HICAT and the intended VMC for the subscale SUSAN aircraft. Speedgoat systems support various input/output (I/O) protocols and are programmed using MATLAB®/Simulink®. Block diagrams can be compiled and executed on the Speedgoat real-time operating system, enabling rapid control algorithm development and deployment.

The propulsion system uses four Jetfan 130 Pro EDFs with TFL56104 550 kV brushless DC inline motors. Wind tunnel testing documented in Ref. [11] demonstrated these EDFs can supply

sufficient thrust for cruise speed and altitude within power constraints for the subscale SUSAN vehicle design. The subscale vehicle is estimated to weigh 1,850 lb, 35% of required thrust is provided by the tail engine and 65% by the wing fans. Thus, each wing fan must deliver 23 lbf to maintain a thrust-to-weight (T/W) ratio of 0.31. This T/W ratio is based on Boeing 737-800 data [13, 14].

The subscale SUSAN vehicle design set the EDF power bus at 75 V, compatible with the motors' maximum settings of 91 V and 150 A. Electronic speed controllers (ESCs) drive the motors. The ESCs communicate with the VMC to receive fan speed commands and send EDF and ESC data. Commercial off the shelf Advanced Power Drives UHV205 ESCs were chosen based on the power bus targets outlined in Ref. [11].

Each EDF is coupled with two brushed DC motors intended to be used for thrust vectoring mechanisms. The ECUs are controlled by microcontroller based distributed control units (DCU). The concept aircraft architecture provides a 24 V bus for the thrust vectoring motors, DCUs, and sensors.

The assembly, as seen in Fig. 1, is based on the proposed electric propulsion setup for the subscale SUSAN vehicle, where the EDF array outlet aligns with the wing's trailing edge. The rig resembles half of the DEP array on the left wing where the VMC and power system sit within the fuselage. On HICAT, the EDFs are fastened to an extruded aluminum T-slot framing rail clamped to a shop table. Electronics attach to a baseboard cut to the dimensions of the wing planform using screws. The ESCs, thrust vectoring motor motor drivers, DCUs, and wiring are arranged to maximize reliability, minimize electromagnetic interference (EMI), simplify manufacturing, and reduce weight for the subscale SUSAN vehicle. Each ECU has its own connection to the power supply to minimize system implications from a single-unit power failure and to reduce EMI by minimizing electrical noise coupling. To further mitigate EMI, power wires are braided, the ESCs are oriented so that high-current wiring is routed clear of command and sensor lines, control signals are routed perpendicularly to power lines, and the ESCs are placed near the EDFs to shorten the wiring between the ESC and EDF which resembles AC power. Finally, components are packed in close proximity so that proposed structure and heat management systems can be shared to keep system weight lower. While the subscale SUSAN aircraft uses a battery-generator power system, HICAT uses DC power supplies (PSs) for power. The HICAT VMC and PSs are located to the left of the assembly in Fig. 1.

3 Hardware Implementation

Detailed hardware specifications for HICAT are critical to system-level engineering performance. This section will expand on the hardware overview presented in the previous section by describing component level characteristics of the testbed. Figure 2 displays one of the four ECUs controlled by the VMC.

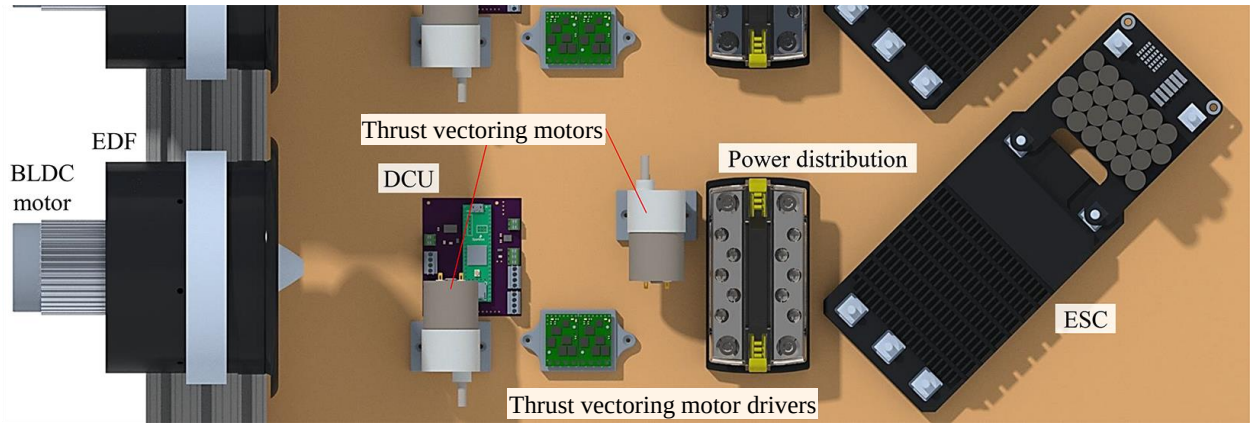

Figure 2: EDF-Control Unit diagram. The thrust vectoring mechanisms are not included on HICAT, the motors for those mechanisms are included to add electrical and control detail to the rig.

3.1 Controller Area Network Communications

The Controller Area Network (CAN) bus protocol serves as the physical communication interface between subsystems and the VMC. CAN bus is defined by a series of standards from the International Organization for Standardization (ISO) titled Road vehicles-Controller area network (ISO11898-1-3) [15–17]. An IO603 Speedgoat® card, which provides up to four high-speed CAN (CAN HS) connections, drives the CAN bus from the VMC. The IO603 is linked to the CAN network using a 9-pin D-sub connector with a screw terminal block. Benefits of CAN include EMI resistance, ease of modification, and bus-wide node-to-node data access with message priorities enforced via identifiable numeric tags (IDs). With all EDFs and thrust vectoring motors, the subscale SUSAN vehicle is planned to use a total of sixty-four hardware nodes on the wing propulsion system. A CAN layout, based on a two-wire main bus with a spoke topology, is much simpler than a pulse-width modulation (PWM) equivalent for a large number of communication nodes.

The ESCs and thrust vectoring control motor drivers lack native CAN support, but are used because they were used previously in SUSAN-related wind tunnel testing in Refs. [11, 12]. Specifically, the ESCs and motor drivers meet power specifications with a safety margin, while the EDFs and thrust vectoring motors satisfy thrust and torque needs, respectively. A microcontroller-based DCU translates CAN signaling to the protocols used by the components. A Teensy® 4.1 is used as the main processing unit for the DCU for its flexible I/O, native CAN handling, and interrupt-pin options. Encoders located on the thrust vectoring motors rely on the interrupt pins to send clocked motor shaft position feedback. The Teensy® offers high speed, low weight, and a compact form factor, but remains programmable with the Arduino development environment. The Teensy® includes an onboard CAN controller, but needs a separate CAN transceiver to drive signals on the bus.

Custom software on the DCU and VMC is required to implement CAN messaging. Figure 3 shows a diagram of the communication system. Basic CAN 2.0 A messaging is used where messages are filtered by ID. CAN messages contain up to eight bytes of data which can be allocated to two four-byte, float data types that represent signed engineering data [18]. An interrupt service routine on the Teensy® filters messages using conditional statements, packages them into byte arrays, and converts them to a union type. Union types store data in memory such that the values can be accessed and defined as multiple data types (e.g., a float or an array) simultaneously. This allows

control algorithms to use a float representation of a value while CAN communication can transmit the same value as a byte array buffer. A First-In-First-Out buffer maintains incoming message integrity. The FlexCANT4 library on the Teensy® handles inbound and outbound CAN messages. To send messages, float-type engineering data from sensors is first cast as a union type. The data, now stored as a union, is retrieved as a byte array and assigned to a buffer structure within a CAN message object. The buffer is then sent on the bus. For Speedgoat® integration, Simulink® blocks handle CAN configuration, as well as CAN message read, decode, write, and encode. A `CAN Decode` block outputs a byte array that is unpacked into floating-point data (single values), whereas a `CAN Encode` block packs float data back into bytes for transmission. The version of CAN used (CAN HS), ID format (standard), and baud rate (500 kbps) are selected on the Teensy® and Speedgoat® to configure the bus.

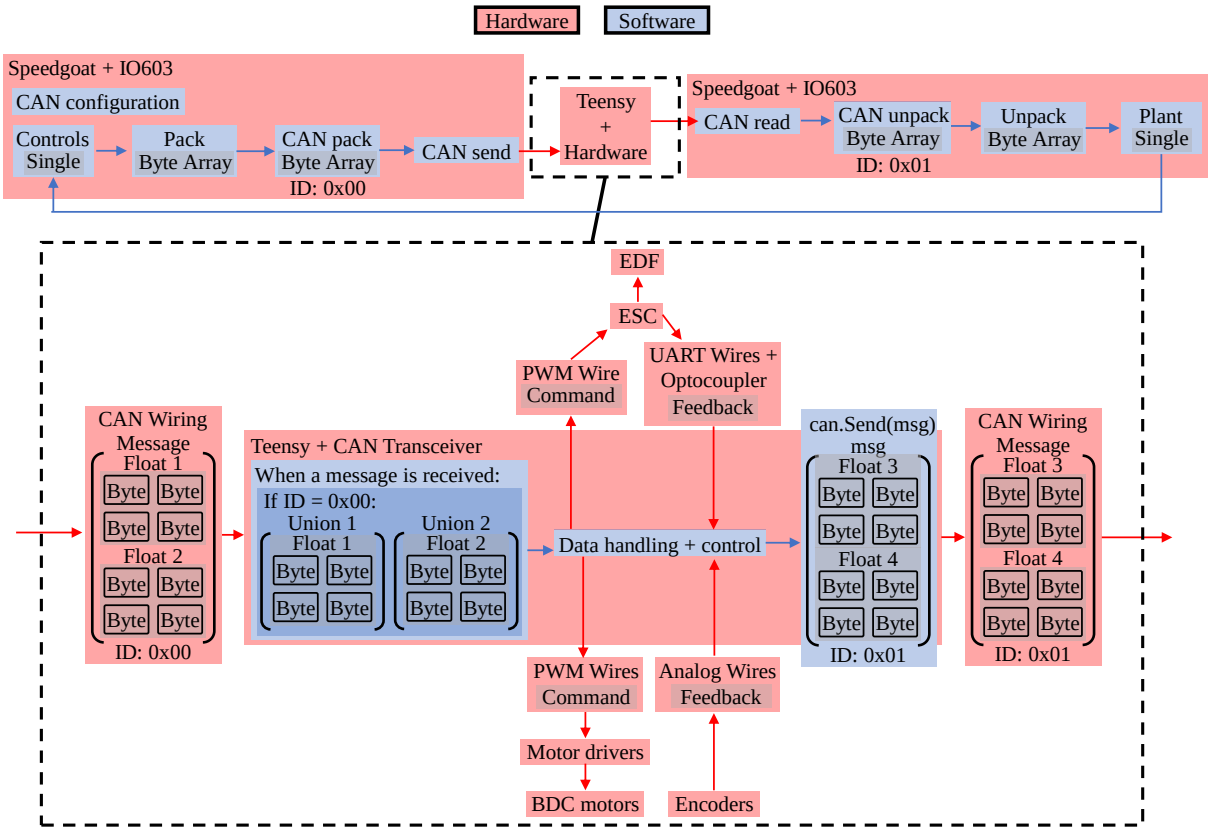

Figure 3: VMC to ECU communication diagram for propulsion and thrust vectoring control through the DCU using CAN messaging.

3.2 Board-based Circuits

The ESCs receive PWM command signals and send feedback data, such as RPM, temperature, current, and duty cycle, over a universal asynchronous receiver/transmitter (UART) serial connection to the DCU. An optoisolator is added to the UART feedback line because the signal is not isolated from the ESC control board. The DCU runs a buffer-handling script to translate the raw

UART byte stream into engineering units like temperature using formulas dependent on the sensors gathering the raw data. A Fletcher checksum maintains incoming buffer integrity.

Brushed DC gear motors are used for the thrust vectoring mechanism motors, driven by motor driver boards that accept two PWM signals from the DCU for throttle and direction. Encoders mounted on the rear of the motor gearbox deliver output shaft position feedback at 9,600 counts per revolution. Each encoder requires four connections to the DCU: two signal wires connected to interrupt pins, and power and ground.

The DCU design, seen in Fig. 4, uses a custom printed circuit board (PCB) to simplify assembly, strengthen wired communication interfaces, and mitigate EMI. The PCB provides a mount for the Teensy®, and screw terminals for secure connections to the ESC, motor drivers, encoders, and CAN bus. The board includes CAN transceiver and optoisolator integrated circuits (IC) to consolidate functionality. Specifically, the MCP2562 transceiver and TLP2770 optoisolator are used. Using a CAN IC mounted to a PCB benefits reliability and functional testing by exposing the termination resistor required by CAN. The placement of the termination resistor is designed to be easily tested with a multimeter.

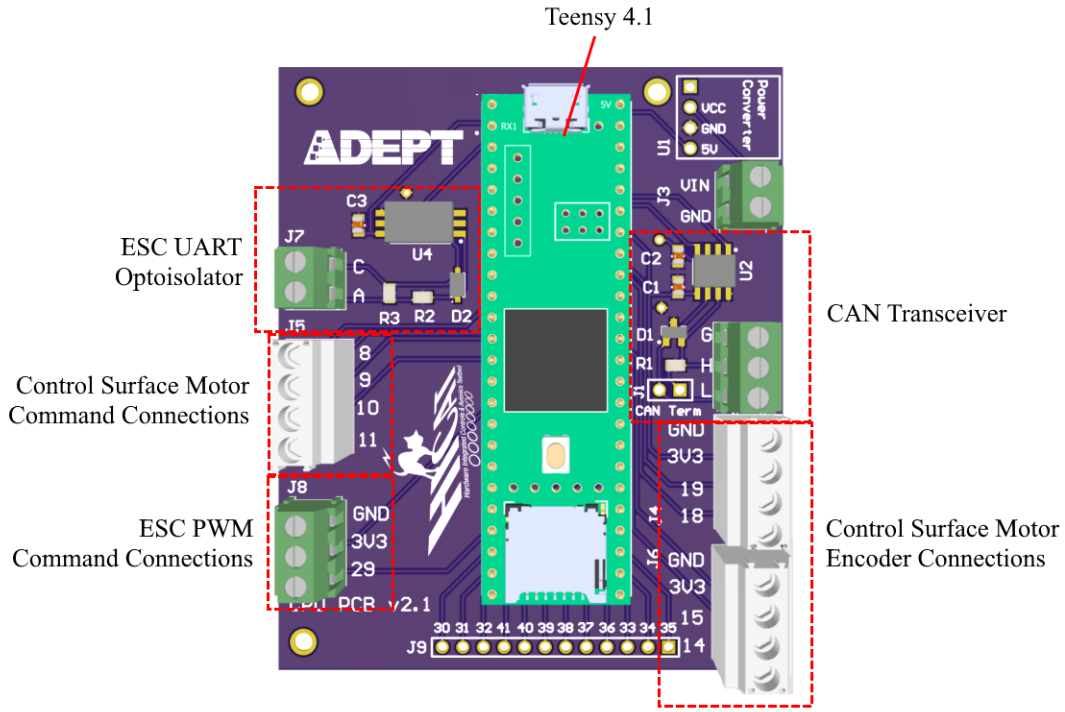

Figure 4: Diagram of the DCU, a custom circuit board used for motor control and CAN message handling.

3.3 Motor Controls

While the ESC and thrust vectoring mechanism motor drivers accept throttle-like inputs (PWM signals), the VMC's commands are best expressed using real-world engineering units (e.g., EDF rotational speed in RPM). The primary method of computing PWM commands from a desired RPM is based on the data shown in Fig. 5. The data are approximated using a continuous piecewise

polynomial function with two separate polynomials mapping RPM to PWM. The lower PWM-RPM regime (1150-1350 μs) uses a third order polynomial map, while the upper regime (1350-1950 μs) uses a first order polynomial. RPM behavior differences between the two PWM regimes arise from electric and mechanical characteristics of the ESC-EDF system. The battery-generator powered subscale SUSAN vehicle may experience voltage drop through flight as power capacity is used, but the data in Fig. 5 is based on a constant supply voltage of 75 V from DC PSs.

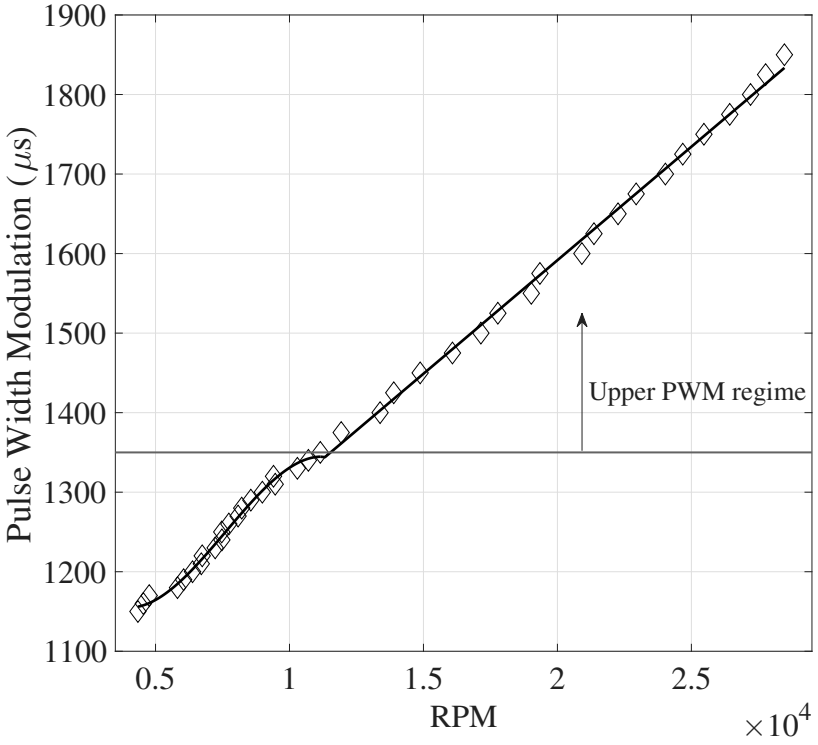

Figure 5: Isolated RPM to PWM data taken at 75 V and 125 A with polynomial fit lines.

A feedback controller is used to track RPM in the upper PWM-RPM regime. The controller changes PWM commands based on error between the target RPM and RPM feedback measured by the ESC. The controller is a proportional-integral (PI) feedback algorithm where gains were tuned using step-response tests to meet desired transient responses. The lower PWM values generate negligible thrust, so there is no operational need to stabilize those commands with a feedback controller. The ESCs accept a limited range of PWM signals (1150-1950 μs), so PWM limits (saturation) are applied before commands are issued. Testing revealed a heuristic anti-windup method should be used to avoid undesired cumulative error growth due to commands being issued in the upper PWM-RPM range while power to the EDFs is turned off. To resolve undesired error growth, the cumulative error in the upper PWM regime controller is reset to zero whenever the lower range controller is active.

A realistic operating mode for the thrust vectoring mechanism (only the motors of which are included in HICAT) would involve commanding a desired mechanism deflection. Each control surface deflection would map to a rotational position of the mechanism motor shaft. This motor position command functionality is implemented using a PI algorithm to track shaft rotational

position. Analog throttle signals are changed by subtracting shaft position feedback measured by the onboard encoder from a desired position command then applying PI gains.

3.4 Power System

Power wiring and distribution blocks were sized using Society of Automobile Engineers (SAE) standards, primarily Wiring Aerospace Vehicles (SAE AS50881H) [19]. Wire gauges were estimated with two methods: a lookup table from SAE AS50881H and a plot-based formula from Fundamentals in Wire Selection and Sizing for Aerospace Applications (SAE AIR6540D) [20]. Additional standards used include Aircraft Electric Power Characteristics (MIL-STD-704F) [21], General Specification for Terminals (SAE AS7928) [22], and Terminal Board Assembly (SAE AS27212D) [23], which informed maximum allowable voltage drop, appropriate terminal connections, and selection of terminal blocks, respectively. The 24 V bus wiring and terminal blocks are over-specified to accommodate growth in the thrust vectoring mechanism motor current ratings. Figure 6 illustrates the power system flow, starting from 110, 208, and 480 V AC (VAC) wall outlets. Three EDFs share a multi-PS system described in Ref. [12], while the fourth EDF is powered by an individual PS, and the 24 V bus is powered by a fifth PS. The fourth EDF is powered by a separate PS because the multi-PS unit only has capacity to fully power three EDFs. The power supplies on the high power bus are set to 75 V DC (VDC), and 125 A. The multi-PS system is expandable, as the units can communicate between one another to pool current when connected in parallel [12].

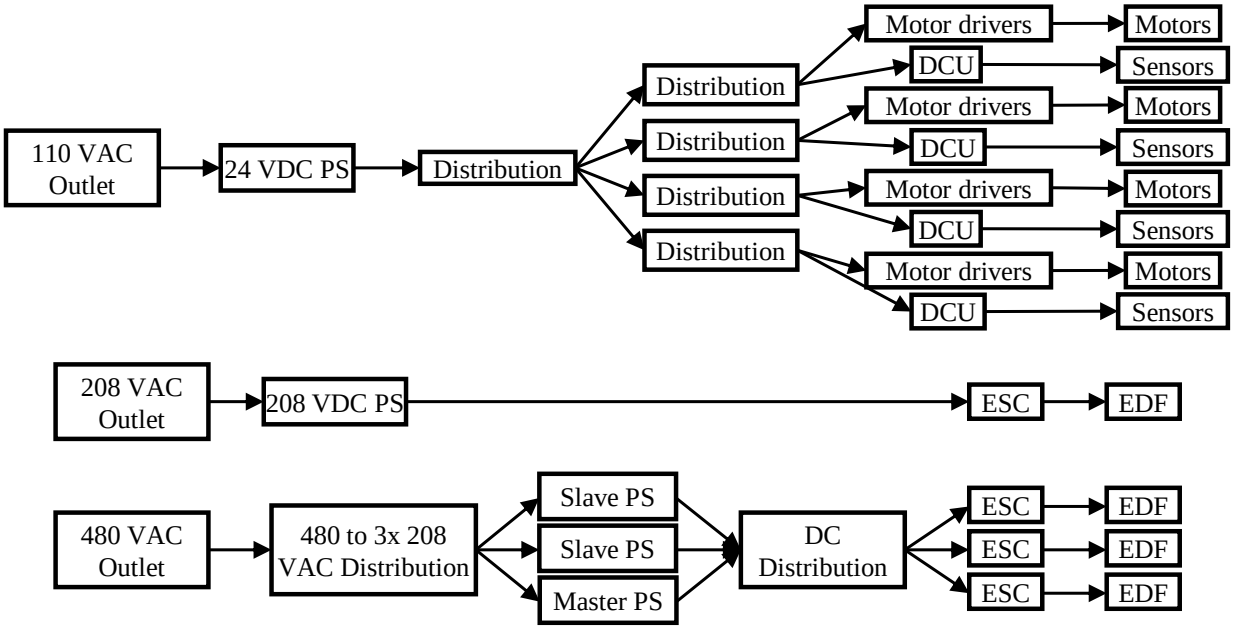

Figure 6: HICAT rig power diagram for ECUs based on DC power supplies.

4 Aircraft Simulation

A flight dynamics simulation is run on the VMC and communicates with a portion of the real propulsion system. The simulation is run on the VMC, alongside the flight control algorithm, for

ease of integration with DEP hardware. The simulation was developed to evaluate the performance of the DEP array with system-level implications, and for control design tasks. Although the subscale SUSAN vehicle informed electronics details, the flight dynamics simulation is based on wind tunnel data from a separate airframe: the commercial transport Common Research Model (CRM). CRM wind tunnel data was used instead of SUSAN data for its availability; a SUSAN airframe was never tested experimentally. The simulation is composed of the aircraft equations of motion and an aerodynamic model implemented in MATLAB®/Simulink®. Associated trim and linearization routines were adapted from the F-16 simulation available in the System IDentification Programs for AirCraft software toolbox [24, 25].

4.1 Equations of Motion

A nonlinear aircraft simulation routine was developed using the kinematic and dynamic aircraft equations of motion under standard assumptions [25–27]. The CRM vehicle is modeled as a single six-degree-of-freedom rigid body subjected to gravitational force, thrust force, and aerodynamic forces and moments. The 12 simulation states are the body-axis translational velocity components (u, v, w), body-axis angular velocity components (p, q, r), Euler angles (ϕ, θ, ψ), and earth-fixed position (x_E, y_E, z_E). Thrust T is assumed to be aligned with the aircraft longitudinal axis, and rotational effects from the aircraft propulsion system are neglected. The translational kinematics equations are:

$$\dot{x}_E = u\cos\theta\cos\psi + v(\sin\theta\cos\psi\sin\phi - \sin\psi\cos\phi) + w(\sin\theta\cos\psi\cos\phi + \sin\psi\sin\phi) \tag{1}$$

$$\dot{y}_E = u\cos\theta\sin\psi + v(\sin\theta\sin\psi\sin\phi + \cos\psi\cos\phi) + w(\sin\theta\sin\psi\cos\phi - \cos\psi\sin\phi) \tag{2}$$

$$\dot{z}_E = -u\sin\theta + v\cos\theta\sin\phi + w\cos\theta\cos\phi \tag{3}$$

The rotational kinematics equations are:

$$\dot{\phi} = p + (q\sin\phi + r\cos\phi)\tan\theta \tag{4}$$

$$\dot{\theta} = q\cos\phi - r\sin\phi \tag{5}$$

$$\dot{\psi} = (q\sin\phi + r\cos\phi)\sec\theta \tag{6}$$

The translational dynamics equations are:

$$\dot{u} = rv - qw - g\sin\theta + \bar{q}SC_X/m + T/m \tag{7}$$

$$\dot{v} = pw - ru + g\cos\theta\sin\phi + \bar{q}SC_Y/m \tag{8}$$

$$\dot{w} = qu - pv + g\cos\theta\cos\phi + \bar{q}SC_Z/m \tag{9}$$

The rotational dynamics equations are:

$$I_x\dot{p} - I_{xz}\dot{r} = \bar{q}SbC_l + (I_y - I_z)qr + I_{xz}pq \tag{10}$$

$$I_y\dot{q} = \bar{q}S\bar{c}C_m + (I_z - I_x)pr + I_{xz}(r^2 - p^2) \tag{11}$$

$$I_z\dot{r} - I_{xz}\dot{p} = \bar{q}SbC_n + (I_x - I_y)pq - I_{xz}qr \tag{12}$$

The aircraft-specific aerodynamics are captured in the force coefficients (C_X, C_Y, C_Z) and moment coefficients (C_l, C_m, C_n) included in the translational and rotational dynamics equations.

4.2 Aerodynamic Model

The CRM aerodynamic model was developed using static and forced oscillation wind tunnel tests performed in the NASA Langley 12-Foot Low-Speed Tunnel [28]. The wind tunnel model was a 2.4% scale version of the original CRM configuration [29] with the ONERA vertical tail design [30, 31]. The model did not include engine nacelles, pylons, or control surfaces. Testing was conducted with and without including the horizontal and vertical tail surfaces.

The longitudinal aerodynamic model equations have the form

$$C_i = C_{i_o}(\alpha) + C_{i_q}(\alpha)\hat{q} + C_{i_{\delta_e}}(\alpha)\delta_e + C_{i_{\delta_f}}\delta_f \tag{13}$$

where "i" is used to represent the X, Z, and m subscripts in C_X, C_Z, and C_m. The $C_{i_o}(\alpha)$ and $C_{i_q}(\alpha)$ parameters vary as a function of α in the form of polynomial equations identified using CRM static and forced oscillation wind-tunnel data [28], respectively. Because control surfaces were not integrated on the wind-tunnel model, control surface effects were approximated using data from the NASA T-2 aircraft. The $C_{i_{\delta_e}}(\alpha)$ parameter was derived from the T-2 model given in Ref. [32], and the $C_{i_{\delta_f}}$ parameter was from estimates of the flap effectiveness presented in Ref. [33].

The lateral-directional aerodynamic model equations have the form

$$C_i = C_{i_\beta}(\alpha)\beta + C_{i_p}(\alpha)\hat{p} + C_{i_r}(\alpha)\hat{r} + C_{i_{\delta_a}}\delta_a + C_{i_{\delta_r}}\delta_r \tag{14}$$

where "i" is used to represent Y, l, and n subscripts for C_Y, C_l, and C_n. The $C_{i_\beta}(\alpha)$ parameter is a polynomial equation identified from static wind-tunnel data; the $C_{i_p}(\alpha)$ and $C_{i_r}(\alpha)$ parameters are polynomial equations developed from forced oscillation wind-tunnel testing. The lateral-directional control surface effectiveness, $C_{i_{\delta_a}}$ and $C_{i_{\delta_r}}$, was approximated from the T-2 model given in Ref. [32].

Sets of aerodynamic model equations with and without the tail surfaces were implemented into the CRM simulation. This was done to allow investigation of using thrust vectoring engines to replace one or both of the tail surfaces with the goal of drag reduction. Although this has not been completed, the simulation allows assessment of these effects in future work.

5 Flight Control Algorithm and Implementation Overview

To verify rapid controls prototyping capability, a linear quadratic regulator (LQR) controller was designed for closed-loop control on the CRM model. LQR is an optimal control approach that produces an optimal gains K based on selected weighing matrices Q, R as a solution of a quadratic cost function. This technique is used in aircraft control due to its inherent robustness and stability guarantees and its ability to easily handle multi-input, multi-output systems [26]. An LQR scheme was designed for the CRM using linearized longitudinal and lateral state space matrices. These state space matrices consider the following states and inputs:

$$\mathbf{x} = \begin{bmatrix} u & v & w & p & q & r & \phi & \theta & \psi \end{bmatrix}^T$$
$$\mathbf{u} = \begin{bmatrix} T & \delta_e & \delta_a & \delta_r \end{bmatrix}^T$$

The longitudinal states are $\mathbf{x}_{\text{lon}} = [u \quad w \quad q \quad \theta]^T$ with longitudinal inputs of thrust and elevator (T, δ_e), whereas the lateral-directional states are $\mathbf{x}_{\text{lat}} = [v \quad p \quad r \quad \phi]^T$ with lateral inputs aileron and rudder (δ_a, δ_r). The gains Q and R are selected based on desired performance goals (i.e. tracking and input regulation). Following selection of Q and R, LQR gains for each axis are determined using the `lqr()` function in MATLAB®. The flying qualities were verified for the closed-loop linear system. The control system performance was assessed using MIL-STD-1797A flying qualities

specifications for cargo aircraft. Level 1 flying qualities were required for the acceptance of the gain K. After producing and evaluating K for the longitudinal and lateral-direction response, the gains are combined into one matrix for control of the nonlinear system such that the total control actuation is:

$$\mathbf{u} = -K\mathbf{x}$$

To accommodate steady state error, an integrator term can be incorporated to regulate tracking error. In this study, the forward velocity error is regulated to assist with tracking and a gain Q_e is used to tune the integrator gain. The weighing matrices used to produce the LQR gains K, K_e were selected to be scaled appropriately to their respective signal units and then adjusted accordingly for desired performance.

Hardware implementation is completed using Simulink® RealTime® to interface with the hardware described in Sections 2 and 3. Because the SUSAN concept vehicle uses sixteen EDFs, and HICAT uses up to four EDFs, the simulation environment duplicates RPM feedback from the real hardware to emulate sixteen EDFs. 1-Fan, 2-Fan, and 4-Fan HICAT configurations were tested, but all of those real configurations emulate a sixteen-EDF vehicle. To implement the duplication functionality, real RPM feedback signals are split into $16/n_{\text{fan}}$, such that each fan represents a fraction of the total number of fans (e.g., in the 4-Fan case, each real EDF represents four simulated EDFs). A flowchart of the process is displayed in Fig. 7. For the present work, uniform allocation is assumed such that the thrust command, T_{cmd}, is divided by sixteen prior to being commanded. After determining T_{cmd}, the value is sent to a lookup table, based on data from Ref. [11], to convert the thrust to an RPM command. The RPM command is sent from the VMC to the fans via the DCU-CAN messaging system. The returning signal, RPM_{act}, is the fan rotational speed measured by the ESCs. The RPM feedback signal is duplicated into sixteen fan speeds, sent to another lookup table based on data from Ref. [11] to convert RPM to single fan actual thrust, and then summed to create a total actual thrust, T_{act}. The total thrust from all fans is then applied to the CRM flight dynamics simulation. Although only uniform thrust was commanded for the work described in this report, a capability to test control allocation methods to distribute thrust non-uniformally is included in the simulation architecture.

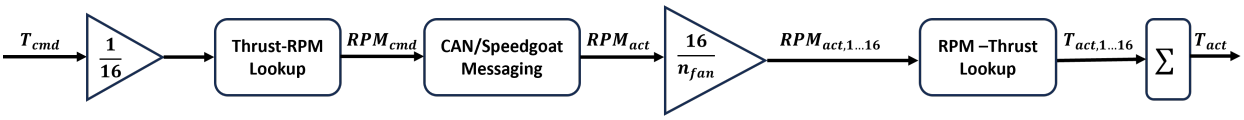

Figure 7: Simulation flowchart connecting the flight control algorithm, lookup tables, and propulsion hardware.

6 Case Study

6.1 Test Setup

The proposed controller is simulated using the CRM dynamic model, with tail surfaces, scaled to the size of the subscale SUSAN vehicle at sea level static environmental conditions. The simulation considers a cruise scenario depicted with a reference forward velocity profile (u_{ref}) where u is used as a proxy for total airspeed V_t. A velocity tracking example was selected to test the propulsion array. The reference profile is designed to mimic a cruise condition with a series of ramp inputs, which permits a trajectory that smoothly ascends or descends towards a new setpoint. The profile, illustrated in Fig. 8, is composed of deviations from u_{trim} starting to simulate cruise velocity changes.

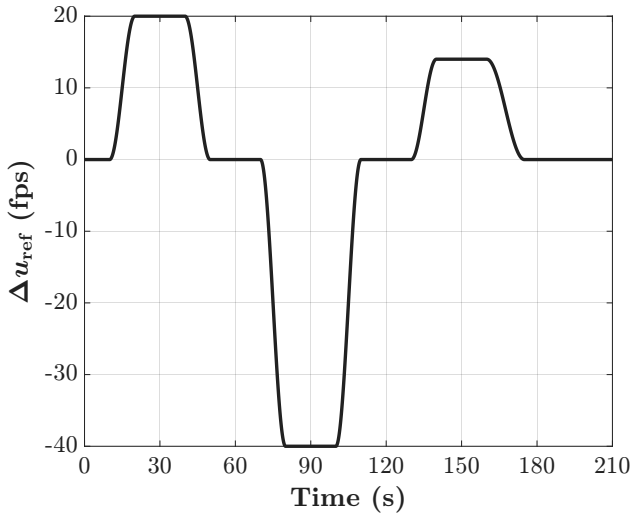

Figure 8: Reference trajectory for u_{ref}.

Tests were run for a total of 240 s with a time step of 0.01 s. Each test includes an initialization period during which the fans are ramped up to a baseline of 10,000 RPM. The target tracking profile is then enabled and runs through 210 s, at which point the fans are ramped down to 10,000 RPM. Consequently, the figures shown focus on the period when the target profile is active. Three fan configurations were considered in testing: 1-Fan, 2-Fan, and 4-Fan. Multiple tests were performed to ensure repeatability of results, however only one run of each configuration is plotted as the authors found negligible variation between each run. As the primary purpose of testing concerns operation and usability of the HICAT setup, closed-loop performance is evaluated only with resultant thrusts, corresponding fan-speeds, and tracking performance. Tracking performance is collected to illustrate the efficacy of the control law to command a thrust, T, and to track the desired trajectory given the fan configurations. Thrust and RPM results are collected to demonstrate commanded versus actuated responses, and to identify potential response differences in the hardware for each fan configuration.

6.2 Results

Figure 9 compares the forward velocity response for a "direct thrust" simulation without DEP hardware and simulations with each fan configuration in the loop to the reference forward velocity trajectory. All configurations follow the reference trajectory reasonably well and exhibit minor steady-state errors during the plateau segments. Figure 10 shows the forward velocity tracking error for each simulation, where similar levels of tracking error ($u_e < 7$ ft/s) is observed for each simulation.

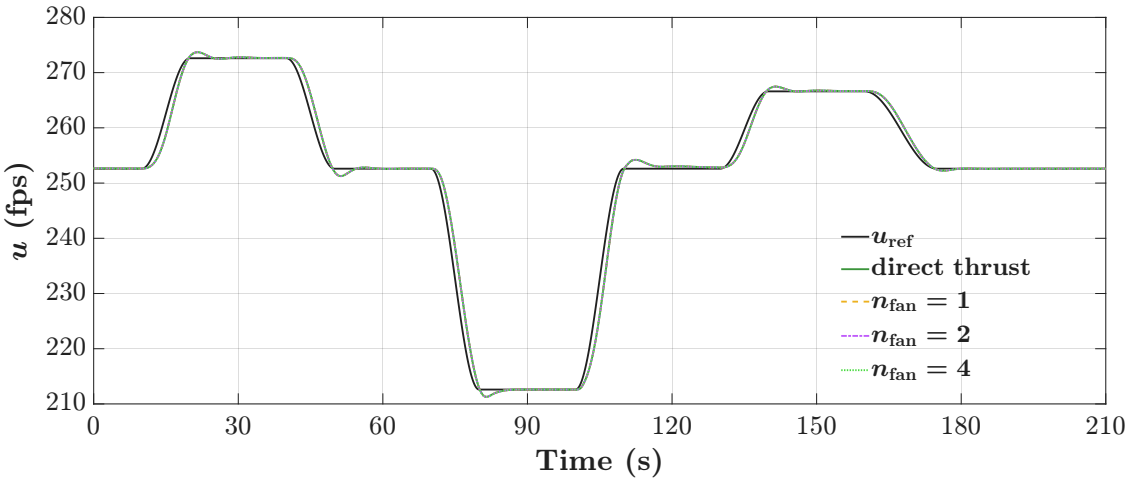

Figure 9: Velocity tracking across fan configurations.

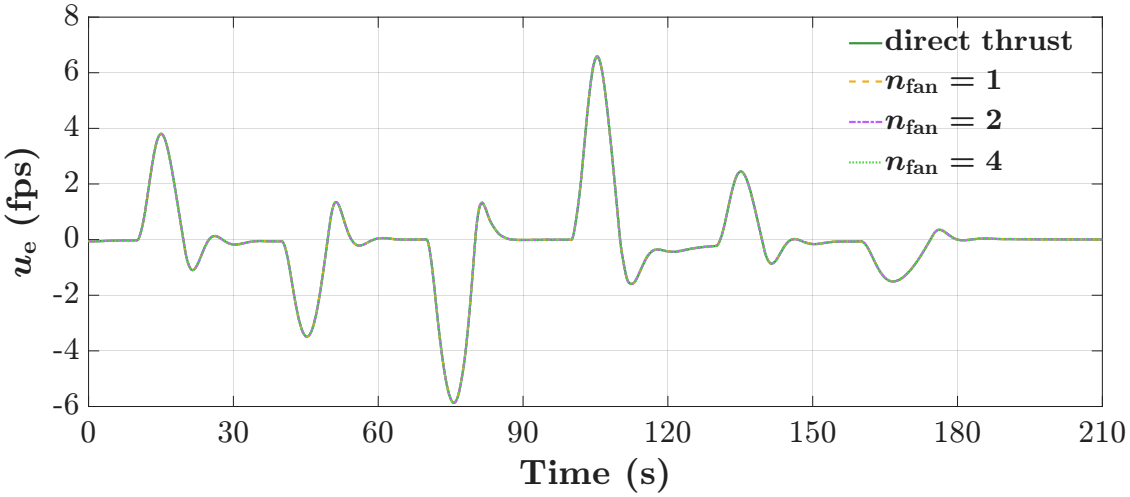

Figure 10: Velocity tracking errors across fan configurations.

Figures 11 and 12 show the thrust and measured individual fan speeds, respectively, for each configuration. Figure 12 provides the measured rotational speed data from EDF hardware used to control the velocity shown in Fig. 9; Fig. 11 shows the corresponding predicted thrust. To improve readability, a low-pass filter was applied to the data to attenuate high-frequency noise.

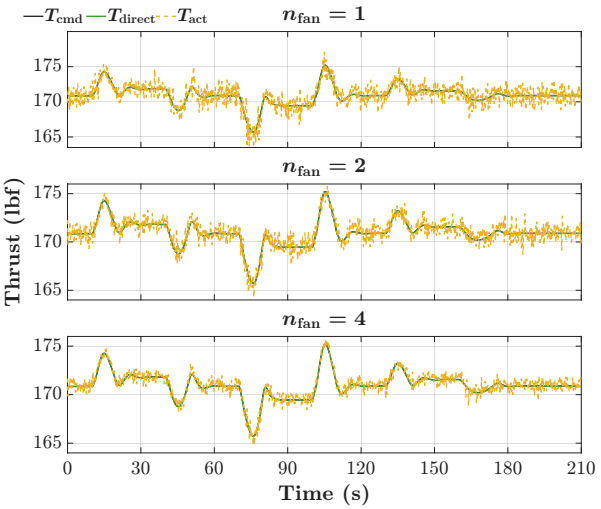

Figure 11: Thrusts for each fan configuration.

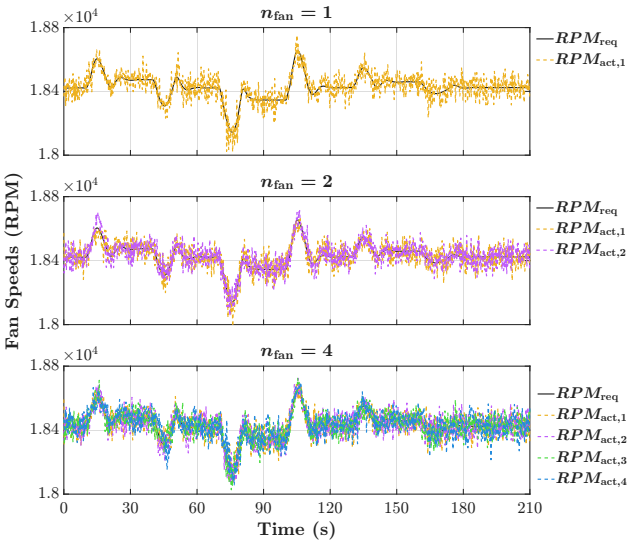

Figure 12: Fan speeds for each fan configuration.

Overall, the commanded thrust, which remains near the thrust trim value of 170.8 lbf, is tracked closely, with minimal discrepancy between T_{cmd} and T_{act}. Figure 12 illustrates each fan appropriately tracks the commanded RPM, and only minor differences exist in the actuated response. The results demonstrate the efficacy of the motor controller described in Section 3, while also confirming the utility of the HICAT setup for rapid flight controls prototyping.

7 Conclusion

HICAT is a rapid controls prototyping testbed developed to advance distributed electric propulsion technology. The SUSAN effort, which initiated development of a DEP-enabled flight research vehicle, informed HICAT's high-level design criteria, including VMC selection, thrust requirements, power-bus specifications, and component layout. To adequately reflect system-level integration effects, HICAT uses flight-like avionics and a representative DEP array layout. Low-level details on the C&DH hardware, motor-driver selection, and motor-control algorithms were refined amidst testing of the DEP hardware. A nonlinear flight dynamics simulation based on wind-tunnel and flight-test data was developed to support propulsion system performance evaluation. The simulation is connected to the propulsion hardware enabling the DEP array to be evaluated as if it were deployed on a flying aircraft. A controller was designed to maintain simulated vehicle forward velocity via a communication link between the simulation and the real propulsion hardware. A commanded velocity profile was successfully maintained in simulation by the real propulsion system showcasing HICAT has a capability for rapid prototyping of controls and avionics.

The work described in this report resulted in substantial progress towards creating a more flight-realistic DEP array testbed. The HICAT setup provides an accurate component layout, a connection between a flight dynamics simulation and hardware, and a high power capacity test capability. HICAT can serve as a general platform for testing high-power avionics with system-integration challenges alongside realistic flight-dynamic modeling. Future enhancements could include incorporating additional subsystems (e.g., control surfaces and sensors), refining the aerodynamics models with new wind-tunnel and flight test data, and investigating alternative control allocation and control law design approaches.

Acknowledgments

This paper is based on work supported by the NASA Aeronautics Research Mission Directorate Convergent Aeronautics Solutions project. The efforts and contributions of several individuals are gratefully acknowledged for participating in the development and execution of these experiments, including Andrew Patterson, Justin Lisee, Earl Harris, Rick Thorpe, Lee Pollard, Mario Smith, Eli Etheridge, and John Inge.

References

1. Chau, T., Kenway, G., and Kiris, C. C., "Conceptual Exploration of Aircraft Configurations for the SUSAN Electrofan," *AIAA SCITECH 2022 Forum,* AIAA 2022-2181, January 2022. https://doi.org/10.2514/6.2022-2181.

2. Jansen, R., Kiris, C. C., Chau, T., Machado, L. M., Duensing, J. C., Mirhashemi, A., Chapman, J., French, B. D., Miller, L., Litt, J. S., Denham, C. L., Lynde, M. N., Campbell, R. L., Hiller, B. R., Blaesser, N. J., and Heersema, N., "Subsonic Single Aft Engine (SUSAN) Transport Aircraft Concept and Trade Space Exploration," *AIAA SCITECH 2022 Forum,* AIAA 2022-2179, January 2022. https://doi.org/10.2514/6.2022-2179.

3. Machado, L. M., Chau, T., Kenway, G. K., Duensing, J. C., and Kiris, C. C., "High-Fidelity Aerodynamic Analysis and Optimization of the SUSAN Electrofan Concept," *AIAA SCITECH 2022 Forum,* AIAA 2022-2304, January 2022. https://doi.org/10.2514/6.2022-2304.

4. Machado, L. M., Chau, T., and Duensing, J., "Toward the Development of an Underwing Boundary Layer Ingesting Distributed Propulsion System for the SUSAN Electrofan," *AIAA SCITECH 2024 Forum,* AIAA 2024-1327, January 2024. https://doi.org/10.2514/6.2024-1327.

5. Chau, T., and Duensing, J., "Conceptual Design of the Hybrid-Electric Subsonic Single Aft Engine (SUSAN) Electrofan Transport Aircraft," *AIAA SCITECH 2024 Forum,* AIAA 2024-1326, January 2024. https://doi.org/10.2514/6.2024-1326.

6. Haglage, J., Dever, T., Jansen, R., and Lewis, M., "Electrical System Trade Study for SUSAN Electrofan Concept Vehicle," *AIAA SCITECH 2022 Forum,* AIAA 2022-2183, January 2022. https://doi.org/10.2514/6.2022-2183.

7. Mirhashemi, A., Chapman, J., Miller, C., Julia, S., and Jansen, R., "Tail-mounted Engine Architecture and Design for the Subsonic Single Aft Engine Electrofan Aircraft," *AIAA SCITECH 2022 Forum,* AIAA 2022-2182, January 2022. https://doi.org/10.2514/6.2022-2182.

8. Litt, J. S., Kratz, J. L., Bianco, S., Sachs-Wetstone, J., Dever, T., Buescher, H. E., Ogden, N. C., Valdez, F., Budolak, D. W., Boucher, M. J., Patterson, A. P., and Jansen, R., "Control Architecture for a Concept Aircraft with a Series/Parallel Partial Hybrid Powertrain and Distributed Electric Propulsion," *AIAA SCITECH 2023 Forum,* AIAA 2023-1750, January 2023. https://doi.org/10.2514/6.2023-1750.

9. Miller, L., and Jansen, R., "Structural Requirements for Design and Analysis of 25% Scale Subsonic Single Aft Engine (SUSAN) Research Aircraft," *AIAA SCITECH 2023 Forum,* AIAA 2023-1939, January 2023. https://doi.org/10.2514/6.2023-1939.

10. Miller, L., "Development of Subsonic Single Aft Engine (SUSAN) Attritable Research Vehicle (SARV) Wing Structure," *AIAA SCITECH 2024 Forum,* AIAA 2024-1523, January 2024. https://doi.org/10.2514/6.2024-1523.

11. Weinstein, R., and Simmons, B. M., "Experimental Characterization of an Electric Ducted Fan for the SUSAN 25% Scale Research Vehicle," *AIAA SciTech 2024 Forum,* AIAA 2024-1524, January 2024. https://doi.org/10.2514/6.2024-1524.

12. Weinstein, R., Spada, V. A., and Simmons, B., "Experimental Study of Aero-Propulsive Interactions for Electric Ducted Fan Arrays in Multiple Positions on a Wing," *AIAA SciTech 2025 Forum,* AIAA 2025-1453, January 2025. https://doi.org/10.2514/6.2025-1453.

13. *Boeing 737 MAX Airplane Characteristics for Airport Planning, Revision H*, Boeing, March 2023. https://www.boeing.com/content/dam/boeing/boeingdotcom/commercial/airports/acaps/737MAX_RevH.pdf, Accessed: 13 August 2025.

14. *LEAP-1B: Type Certificate Data Sheet Issue 8*, European Union Aviation Safety Agency, December 2022. https://www.easa.europa.eu/en/document-library/type-certificates/engine-cs-e/easae115-leap-1b-series-engines, Accessed: 13 August 2025.

15. *Road vehicles - Controller area network (CAN) - Part 1: Data link layer and physical coding sublayer*, ISO - International Organization for Standardization, Chemin de Blandonnet 8, CP 401, 1214 Vernier, Geneva, Switzerland, May 2024.

16. *Road vehicles - Controller area network (CAN) - Part 2: High-speed physical medium attachment (PMA) sublayer*, ISO - International Organization for Standardization, Chemin de Blandonnet 8, CP 401, 1214 Vernier, Geneva, Switzerland, March 2024.

17. *Road vehicles - Controller area network (CAN) - Part 3: Low-speed, fault-tolerant, medium-dependent interface*, ISO - International Organization for Standardization, Chemin de Blandonnet 8, CP 401, 1214 Vernier, Geneva, Switzerland, June 2006.

18. *IEEE Standard for Floating-Point Arithmetic*, IEEE - The Institute of Electrical and Electronics Engineers, Inc., IEEE Service Center, 445 Hoes Lane, Piscataway, NJ 08855-1331, June 2019. https://ieeexplore.ieee.org/document/8766229, Accessed: 16 August 2025.

19. *SAE AS50881H - Wiring Aerospace Vehicles*, SAE International, 400 Commonwealth Drive, Warrendale, PA, 15096-0001, USA, January 2023.

20. *SAE AIR6540D - Fundamentals in Wire Selection and Sizing for Aerospace Applications*, SAE International, 400 Commonwealth Drive, Warrendale, PA, 15096-0001, USA, March 2025.

21. *MIL-STD-704F CHANGE 1 - Aircraft Electric Power Characteristics*, Naval Air Systems Command, Commander, Naval Air Systems Command, Systems Standardization Division, Code 4.1.2, Mail Stop 120-3, Route 547, Joint Base MDL, NJ, USA, December 2016.

22. *SAE AS7928 - Terminals, Lug: Splices, Conductor: Crimp Style, Copper, General Specification for*, SAE International, 400 Commonwealth Drive, Warrendale, PA, 15096-0001, USA, June 1999.

23. *SAE AS27212D - Terminal Board Assembly, Molded-In-Stud, Electric*, SAE International, 400 Commonwealth Drive, Warrendale, PA, 15096-0001, USA, June 2019.

24. *System IDentification Programs for AirCraft, SIDPAC*, NASA Technology Transfer Program, 2025. https://software.nasa.gov/software/LAR-16100-1, Accessed: 12 August 2025.

25. Morelli, E. A., and Klein, V., *Aircraft System Identification: Theory and Practice*, 2nd ed., Sunflyte Enterprises, Williamsburg, VA, 2016.

26. Stevens, B. L., Lewis, F. K., and Johnson, E. N., *Aircraft Control and Simulation: Dynamics, Controls Design, and Autonomous Systems*, 3rd ed., Wiley, Hoboken, NJ, 2016.

27. Etkin, B., and Reid, L. D., *Dynamics of Flight: Stability and Control*, 3rd ed., John Wiley & Sons, Inc, New York, NY, 1996.

28. Vicroy, D. D., and Farrell, S. M., "NASA Langley Flight Dynamics Check Standard Tests," NASA Report, To be published.

29. Vassberg, J., Dehaan, M., Rivers, M., and Wahls, R., "Development of a Common Research Model for Applied CFD Validation Studies," *26th AIAA Applied Aerodynamics Conference,* AIAA 2008-6919, August 2008. https://doi.org/10.2514/6.2008-6919.

30. Cartieri, A., Hue, D., Chanzy, Q., and Atinault, O., "Experimental Investigations on the Common Research Model at ONERA-S1MA – Comparison with DPW Numerical Results," *55th AIAA Aerospace Sciences Meeting,* AIAA 2017-0964, January 2017. https://doi.org/10.2514/6.2017-0964.

31. Hue, D., Péron, S., Wiart, L., Atinault, O., Gournay, E., Raud, P., Benoit, C., and Mayeur, J., "Validation of a near-body and off-body grid partitioning methodology for aircraft aerodynamic performance prediction," *Computers & Fluids*, Vol. 117, 2015, pp. 196–211. https://doi.org/10.1016/j.compfluid.2015.05.021.

32. Grauer, J. A., and Morelli, E. A., "Generic Global Aerodynamic Model for Aircraft," *Journal of Aircraft*, Vol. 52, No. 1, 2015, pp. 13–20. https://doi.org/10.2514/1.C032888.

33. Morelli, E. A., "Flight Test Maneuvers for Efficient Aerodynamic Modeling," *Journal of Aircraft*, Vol. 49, No. 6, 2012, pp. 1857–1867. https://doi.org/10.2514/1.C031699.